Inelastic scattering from core electrons: A multiple scattering approach

J. A. Soininen,[1,2] A. L. Ankudinov,[2] and J. J. Rehr[2]
[1]*Division of X-ray Physics, Department of Physical Sciences, University of Helsinki, FIN-00014 Finland*
[2]*Department of Physics, University of Washington, Seattle, Washington 98195-1560, USA*
(Received 17 March 2005; published 21 July 2005)

The real-space multiple-scattering approach is applied to model nonresonant inelastic scattering from deep core electron levels over a broad energy spectrum. This approach is applicable to aperiodic or periodic systems alike and incorporates *ab initio*, self-consistent electronic structure and final state effects. The approach generalizes to finite momentum transfer a method used extensively to model x-ray absorption spectra (XAS), and includes both near-edge spectra and extended fine structure. The calculations can be used to analyze experimental results of inelastic scattering from core electrons using either x-ray photons or electrons. In the low momentum transfer region (the dipole limit), these inelastic loss spectra are proportional to those from XAS. Thus, their analysis can provide similar information about the electronic and structural properties of a system. Results for finite momentum transfer yield additional information concerning monopole, quadrupole, and higher couplings. Our results are compared both with experiment and with other theoretical calculations.

DOI: 10.1103/PhysRevB.72.045136 PACS number(s): 79.20.Uv, 78.70.Ck, 71.15.Qe

I. INTRODUCTION

The primary aim of this work is to model inelastic scattering quantitatively using a generalization of the real-space multiple scattering (RSMS) approach. This *ab initio* Green's function method has been extensively developed for calculations of x-ray absorption spectra (XAS) and related spectroscopies.[1,2] Thus, the approach permits calculations of inelastic scattering in arbitrary aperiodic materials over a broad energy range, including the near-edge and extended fine structure. In inelastic scattering experiments, the scattering cross section is measured as a function of the energy ω and momentum $\mathbf{q}$ transferred from the probe to the system (throughout this paper we use Hartree atomic units, $e=\hbar=m=1$). When the energy transfer is close to the binding energy of a core state, the inelastic scattering cross section exhibits pronounced jumps, from which one can study the core-excited states of the system. We focus in this paper on the excitations from such core levels.

In the low momentum transfer regime the scattering cross section is dominated by the dipole allowed excitations. Qualitatively the dipole approximation is valid when $qa \ll 1$, where $a \sim 1/\zeta$ is the mean radius of the core state, ζ being the effective core charge. In the dipole limit the inelastic scattering cross section is proportional to the x-ray absorption coefficient,[3–5] and the direction $\hat{\mathbf{q}}$ of the momentum transfer vector plays the role of the XAS polarization vector $\hat{\boldsymbol{\epsilon}}$. Thus, the anisotropy of the x-ray edge can be studied by varying $\hat{\mathbf{q}}$ in much the same way it is studied in XAS by varying the direction of $\hat{\boldsymbol{\epsilon}}$. However, as the magnitude of q increases, contributions from other (dipole forbidden) excitation channels become important. The symmetries of a system generally restrict the available excitation channels at a given excitation energy. The relative weights of the various excitation channels, as a function of momentum transfer, also depend on the spatial extent of the excited state. In general, the classification of the spectral features into given spatial symmetries of the final state electron (i.e., *s*-type, *p*-type, etc.) is not as straightforward as in XAS. This is because contributions to the spectra from different excitations often overlap at finite momentum transfer. Due to this overlap, a detailed analysis of experimental results can be difficult in the absence of quantitative theoretical calculations. There are some exceptions though; core excitons can have well-defined spatial symmetries and energies well separated from other excitations.

Nonresonant inelastic scattering spectra can be measured using either electron energy-loss spectroscopy (EELS)[6] or nonresonant inelastic x-ray scattering (NRIXS).[7] The cross sections in both cases are related to the dynamic structure factor $S(\mathbf{q},\omega)$ of the system. For the case of x rays, the nonrelativistic Born approximation for the NRIXS double-differential cross section is[8,9]

$$\frac{d^2\sigma}{d\Omega d\omega} = \left(\frac{d\sigma}{d\Omega}\right)_{Th} S(\mathbf{q},\omega). \tag{1}$$

Here $(d\sigma/d\Omega)_{Th}$ is the Thomson scattering cross section. The Thomson cross section can be expressed in terms of the incoming (scattered) photon polarization vector and energy $\{\hat{\boldsymbol{\epsilon}}_1,\omega_1\}(\{\hat{\boldsymbol{\epsilon}}_2,\omega_2\})$ as

$$\left(\frac{d\sigma}{d\Omega}\right)_{Th} = r_0^2(\hat{\boldsymbol{\epsilon}}_1\cdot\hat{\boldsymbol{\epsilon}}_2)^2\frac{\omega_2}{\omega_1},$$

where r_0 is the classical electron radius. In Eq. (1) we have implicitly assumed that the energy of the incident x ray is not close to any core binding energy E_i (typically $E_i \ll \omega_1$). This is in contrast with resonant inelastic x-ray scattering experiments, where the incident x-ray energy is tuned close to a core binding energy and resonant processes dominate the double-differential cross section. The different forms of inelastic x-ray scattering and their relationships are discussed in more detail in Refs. 8 and 9. In EELS the corresponding scattering cross section in the Born approximation is[10]

$$\frac{d^2\sigma}{d\Omega d\omega} = \left(\frac{d\sigma}{d\Omega}\right)_{e-e} S(\mathbf{q},\omega), \quad (2)$$

where $(d\sigma/d\Omega)_{e-e}=4q^{-4}(p'/p)$ is the electron-electron scattering cross section, with p (p') being the momentum of the incoming (scattered) electron. In other words, with these approximations the cross sections differ only by a coupling constant which is related to the probe (i.e., a photon or electron) that interacts with the system. The system-dependent part, namely the dynamic structure factor $S(\mathbf{q},\omega)$, is the same for both NRIXS and EELS, and depends only on the structure and excited-state properties of the system under investigation.

Nonresonant inelastic x-ray scattering from core-excited states is often called x-ray Raman scattering (XRS). Traditionally, XRS experiments have been limited to K edges of low-Z materials. However, for the K edges, experimentally accessible systems include such important cases as those with carbon and oxygen, as has already been demonstrated (see Ref. 12 and references therein). Recently, XRS experiments were done for the L edges and N edges of materials with higher Z including the N edge of Ba in Ba_8Si_{46}.[11] The smallness of the x-ray scattering cross section implies that bulk information is generally obtained in these probes, i.e., that multiple scattering of the probe particles and surface effects are usually not serious problems. XRS has been used to study both the momentum transfer magnitude[13–17] and direction dependence[17] at K edges. Recently, the K edge of Be metal was studied using both degrees of freedom (magnitude and direction).[18] The typical energy resolution of current XRS experiments is around 1.0 eV FWHM, although some experiments with an energy resolution of 0.4 eV have been carried out.[13] The finite core-hole lifetime broadening also limits the useful energy resolution to a few tenths of an electron volt.

As noted above, one can also measure the fine structure of the spectra above deep core edges using electrons as a probe. Unlike nonresonant x-ray scattering, EELS is not limited to low-Z materials, and has a typical energy resolution on the order of 0.1 eV. Electrons interact strongly with solids, so that one is often able to obtain results with good statistical accuracy. However, their strong interaction also implies that multiple scattering of the probe electrons can be a problem which has to be removed or otherwise accounted for in the analysis of experimental results. This is especially true of experiments with large scattering angles or low incident electron energies, in which case one should explicitly include multiple scattering in the analysis, as explained in Refs. 19, 20. The dependence of x-ray edges on the magnitude of the momentum transfer has been investigated in Refs. 6, 21, and 22, and more recently in Ref. 23. The dependence on the momentum transfer direction at x-ray edges has also been used in the analysis of anisotropy of x-ray edges (see Refs. 24, 25 and references therein). Additionally, the very high spatial resolution available in EELS makes it possible to study the anisotropy of x-ray edges in fine-grained solids.[25]

Theoretically the problem of calculating inelastic scattering spectra from core-excited states is analogous to the calculation of core level x-ray absorption, the main difference being in the nature of the transition matrix elements. Thus, there are a number of effects that must be taken into account for accurate computational results. Within the independent electron approximation, the main problem is the behavior of the core-excited final states. This can be approached either by calculating the core-excited states one by one (e.g., in band-structure- or molecular-orbital-based approaches) or equivalently, by calculating the one-electron Green's function for the excited states, as is done in this work. For accurate results one needs a highly quantitative method for calculating single-particle properties such as electron densities and Coulomb potentials. Also, a number of many-body properties of the excited states of the system have to be considered. These include the interaction of the final-state electron with the core hole created in the excitation process, as well as an approximation for the energy-dependent self-energies $\Sigma(E)$ of both the electron and the core hole, e.g., to account for inelastic losses. A good approximation in many cases is to calculate the final state in the presence of the core hole and the initial state with ground-state potentials.[1] This approximation is referred to as the *final state rule*. In principle one should include the whole energy dependence of the self-energy, as discussed for example in Ref. 26. However, often a quasiparticle approximation is used both for the electron and the core hole. In the quasiparticle approximation, the imaginary part of the self-energy causes the electron (and the hole) in the excited state to have a finite lifetime. Additionally, the real part of the self-energy shifts the spectral features from the positions predicted by ground state (or mean-field) approximations, whereas traditional ground-state density functional treatments can lead to significant errors in peak positions and intensities. For a full treatment, especially at high energies, one also needs to consider coupling to vibrational degrees of freedom, which give the spectra a temperature-dependent damping comparable to that of x-ray Debye-Waller factors. A more detailed review of the problem of computing core-excited states in XAS can be found in Ref. 1. As noted above, the main difference between inelastic scattering and x-ray absorption lies in the transition matrix elements. This is due to the fact that the operator mediating the transitions in inelastic scattering is $\exp(i\mathbf{q}\cdot\mathbf{r})$, as compared to the dipole operator $\hat{\boldsymbol{\varepsilon}}\cdot\mathbf{r}$ (and, in some cases, also the quadrupole operator) in x-ray absorption. We will discuss this difference in more detail below.

In this paper we have applied the real-space multiple-scattering (RSMS) approach to calculate the core-excited states in EELS and NRIXS over a wide energy range. The RSMS approach adopted here is essentially an effective, independent particle approach for excited states which takes into account the most important final-state effects. The approach is an extension of the RSMS approach previously used for x-ray absorption spectra (see for example Ref. 1 and references therein). The RSMS approach can also be extended to situations where many-particle effects have to be taken into account more accurately than is possible using an effective single-particle approach.[27–30] The momentum transfer dependence of both the near-edge spectra and the fine structure in inelastic loss spectra is analyzed in detail and compared with experimental results.

Recently, a two-particle approach to core-excited states has been developed[31,32] based on the Bethe-Salpeter equation

(BSE). The BSE goes beyond the independent particle approximation with an explicit treatment of the screened electron core-hole interaction. However, when the core-hole interaction is strong, the results from the final-state rule can be comparable.[33] The BSE approach has been applied to different situations using the momentum transfer-dependent matrix elements in the analysis of XRS.[14,15,18,32] For completeness, our calculations are also compared with calculations based on the BSE. However, the BSE approach is currently applicable only relatively close to a given edge, typically between a few tens and 100 eV depending on the material, and becomes computationally impractical for treating the extended fine structure in inelastic scattering spectra.

II. REAL-SPACE MULTIPLE-SCATTERING FORMALISM

A. Green's function formulation

We now briefly describe the extension of the real-space multiple-scattering approach for calculations of nonresonant inelastic scattering. The RSMS approach can be regarded as the real-space analog of the Korringa-Kohn-Rostoher (KKR) band structure method,[34] but unlike KKR, the method makes no assumption of symmetry and is applicable to periodic and aperiodic systems alike. Moreover, the implementation used here is an *all-electron* approach which can be applied to arbitrary systems throughout the periodic table. This method has been extensively developed for *ab initio* calculations of x-ray spectra including both EXAFS (extended x-ray absorption fine structure) and XANES (x-ray absorption near-edge structure).[1,2,27] Its generalization here to finite momentum transfer $\mathbf{q}$ is relatively straightforward, though nontrivial in several respects, as discussed below. We will rewrite the dynamic structure factor in a form that makes it suitable for analysis using concepts and ideas familiar from the RSMS work on XAS.[1,2,27] This is not done only to use the modeling experience obtained from studies on XAS but also to show how inelastic scattering can be used to obtain new information. The contributions to $S(\mathbf{q},\omega)$ from excitations from a tightly bound core state $|i\rangle$ can be approximated using Fermi's golden rule, i.e.,

$$S_i(\mathbf{q},\omega) = \sum_f |\langle f|e^{i\mathbf{q}\cdot\mathbf{r}}|i\rangle|^2 \delta(\omega + E_i - E_f), \tag{3}$$

where E_i (E_f) is the initial (final) state quasiparticle energy of the electron. For the remainder of the paper we will drop the index i and use simply $S(\mathbf{q},\omega)$ when referring to the contribution from a core state $|i\rangle$. Within the one-electron approximation and the final-state rule, the final (photoelectron) states $|f\rangle$ are quasiparticle states which are eigenfunctions of the final-state Hamiltonian in the presence of an adiabatically screened core hole (denoted with a prime), i.e., $H' = p^2/2m + V'_{\text{coul}} + \Sigma(E)$. Here, $\Sigma(E)$ is the self-energy (or dynamically screened exchange-correlation potential) which accounts for inelastic losses, which are essential for a proper treatment of inelastic electron scattering. In our calculations we use the energy-dependent local density approximation for $\Sigma(E)$ of Hedin and Lundqvist,[35] based on the plasmon-pole approximation for the dielectric function. This approximation is usually adequate at moderate to high photoelectron energies.[1] The states $|i\rangle$ are deep core levels of the initial state Hamiltonian without a core hole. For small momentum transfers in the case of core-excited states, the excitation operator $\exp(i\mathbf{q}\cdot\mathbf{r})$ can be expanded as

$$\exp(i\mathbf{q}\cdot\mathbf{r}) \approx 1 + i\mathbf{q}\cdot\mathbf{r} + O(q^2). \tag{4}$$

Thus, the dipole selection rule is approximately valid at small q, since the first term should not contribute to transitions due to orthogonality of the initial and final states, and the next term ($\propto q^2$) is also small. In fact, since ω and $\mathbf{q}$ can, in principle, be chosen separately, the dipole approximation can sometimes be satisfied better in inelastic scattering than in absorption, where the photon momentum and energy are always linked. At higher q, dipole forbidden transitions become important, and it is more convenient to expand the exponential in terms of spherical harmonics

$$\exp(i\mathbf{q}\cdot\mathbf{r}) = 4\pi \sum_{lm} i^l j_l(qr) Y^*_{lm}(\hat{\mathbf{q}}) Y_{lm}(\hat{\mathbf{r}}). \tag{5}$$

Thus, for any finite momentum transfer all excitation channels are present.

To avoid explicit calculations of final states, it is advantageous to re-express the golden rule in terms of the one-particle Green's function or propagator $G = [E - H' + i\Gamma]^{-1}$ in real space, where Γ is the core-hole lifetime. Thus, using the spectral representation, $-(1/\pi)\text{Im}\, G(E) = \Sigma_f |f\rangle\langle f| \delta(E - E_f) \equiv \rho(E)$, the dynamic structure factor becomes

$$S(\mathbf{q},\omega) = \langle i|e^{-i\mathbf{q}\cdot\mathbf{r}'} P \rho(\mathbf{r}',\mathbf{r},E) P e^{i\mathbf{q}\cdot\mathbf{r}}|i\rangle, \tag{6}$$

where the photoelectron energy is $E = \omega + E_i$. The operator P projects the Green's function onto the unoccupied states of the initial state (without the core hole) Hamiltonian.[26] The operator P is needed here since, in general, the eigenstates of the final-state Hamiltonian are not strictly orthogonal to the initial states. In practice, this nonorthogonality implies that at low momentum transfer

$$\langle i|e^{-i\mathbf{q}\cdot\mathbf{r}}|f\rangle \approx \langle i|f\rangle - i\langle i|\mathbf{q}\cdot\mathbf{r}|f\rangle + \cdots. \tag{7}$$

Thus, the dipole forbidden excitations, which incorrectly vary as $\propto\langle i|f\rangle$, can begin to dominate over the dipole allowed transitions $\propto q$ as $q \to 0$. The application of the full projection operator P would require taking an inner product and appropriate matrix elements of all the occupied states $|j\rangle$ of the initial state Hamiltonian, i.e.,

$$P e^{i\mathbf{q}\cdot\mathbf{r}}|i\rangle = e^{i\mathbf{q}\cdot\mathbf{r}}|i\rangle - \sum_j^{occ} |j\rangle\langle j|e^{i\mathbf{q}\cdot\mathbf{r}}|i\rangle. \tag{8}$$

Instead, we simply approximate the effect of P by modifying the excitation operator as

$$\tilde{P} e^{i\mathbf{q}\cdot\mathbf{r}}|i\rangle \approx [e^{i\mathbf{q}\cdot\mathbf{r}} - \langle i|e^{i\mathbf{q}\cdot\mathbf{r}}|i\rangle]|i\rangle. \tag{9}$$

Clearly, at low momentum transfers this gives matrix elements

$$\langle i|e^{-i\mathbf{q}\cdot\mathbf{r}}\tilde{P}|f\rangle \approx -i\langle i|\mathbf{q}\cdot\mathbf{r}|f\rangle + \Theta(q^2), \tag{10}$$

while at high momentum transfers the correction $\langle i|e^{i\mathbf{q}\cdot\mathbf{r}}|i\rangle \times\langle f|i\rangle$ approaches zero. Although in what follows we do not explicitly include the operator $\tilde{P}$, it is included in the actual calculations. The terms coming from the difference of P and $\tilde{P}$ are neglected. Although this is a somewhat uncontrolled approximation, comparison with experiments and previous XRS calculations at different momentum transfers show that these terms should be small, as illustrated in Fig. 2 below. Also, work in XAS suggests that the difference is not significant compared with other theoretical uncertainties.[26]

In multiple scattering (MS) theory, the scattering perturbation is the total electron potential, which is separated into contributions from "scattering potentials" v_R which are localized on each atomic site $\mathbf{R}$, i.e.,

$$V'_{\text{coul}} + \Sigma(E) = \sum_R v_R(\mathbf{r}-\mathbf{R}). \tag{11}$$

In the RSMS method $v_R(\mathbf{r})$ is usually taken to be spherically symmetric. This is a good approximation for electron scattering calculations at moderate electron kinetic energies, i.e., a few electron volts above the threshold. These potentials are calculated self-consistently by iterating the total electron density, potential and Fermi energy, typically requiring about 10–20 iterations. Once the potentials are known, scattering phase shifts δ_l are calculated and dimensionless t matrices evaluated using the relation $t_l=\exp(i\delta_l)\sin(\delta_l)$. With spherically symmetric potentials, the propagator $G(E)$ [and hence the density matrix $\rho(E)$] can be represented in an angular-momentum $L=(l,m)$ and site $\mathbf{R}$ basis $|L,\mathbf{R}\rangle$. Thus, at the site of the core-excited atom ($\mathbf{R}=\mathbf{0}$)

$$\rho(\mathbf{r}',\mathbf{r},E) = \sum_{L,L'} R_L(\mathbf{r},E)\rho_{L,L'}(E)R_{L'}(\mathbf{r}',E), \tag{12}$$

where $R_L(\mathbf{r},E)$ are scattering states at energy E, which are regular at the origin. The expansion for $\mathbf{r}$ and $\mathbf{r}'$ about different sites $\mathbf{R}$ and $\mathbf{R}'$ is similar, with $G_{L,L'}(E)$ replaced by $G_{L\mathbf{R},L'\mathbf{R}'}(E)$. Consequently, the calculation of the dynamic structure factor is reduced to a calculation of (embedded) atomic transition matrix elements $M_L(\mathbf{q},E)=\langle R_L(E)|e^{i\mathbf{q}\cdot\mathbf{r}}|i\rangle$ and a multiple-scattering matrix $\rho_{L,L'}(E)=\rho_{L\mathbf{0},L'\mathbf{0}}(E)$, i.e.,[36]

$$S(\mathbf{q},\omega) = \sum_{LL'} M_L(-\mathbf{q},E)\rho_{L,L'}(E)M_{L'}(\mathbf{q},E). \tag{13}$$

Here $\rho_{L,L'}(E)=(-1/\pi)\text{Im}\, G_{L,L'}(E)$ denote matrix elements of the final-state density matrix, including the effect of the core-hole potential. It can be shown that $S(\mathbf{q},\omega)$ also satisfies a generalized oscillator strength sum rule. The representation in Eq. (13) shows that the essential physics of the problem separates into two parts: (i) a $\mathbf{q}$-dependent transition matrix which governs the production of photoelectrons into various final states, and (ii) a propagator matrix $G_{L,L'}$ which describes the scattering of the photoelectron within the system at a given excitation energy. The transition matrix elements $M_L(\mathbf{q},E)$ are calculated using the expansion in Eq. (5) of $\exp(i\mathbf{q}\cdot\mathbf{r})$ in terms of spherical harmonics. Depending on the excitation energy and momentum transfer, different terms L in this expansion are important. For low momentum transfer and excitation energy, the small Δl transitions are most important, starting from the dipole $\Delta l=\pm 1$, monopole $\Delta l=0$, and quadrupole $\Delta l=\{\pm 2,0\}$ transitions. Thus, provided one can neglect the coupling to phonons (which is a good approximation for core excitations discussed in this work), a typical spectrum at low q can be analyzed using only these three excitation channels. Monopole transitions, which are present in $S(\mathbf{q},\omega)$ through the term $\propto 4\pi j_0(qr)Y^*_{00}(\hat{\mathbf{q}})Y_{00}(\hat{\mathbf{r}})$, have no counterpart in absorption (s-to-s transitions being forbidden within the dipole approximation). When the momentum transfer is increased in inelastic scattering, other excitation channels become more important, especially at high energy values.

The above RSMS formulation can be advantageous even for crystals, since periodicity is broken by the core-hole interaction and spectral broadening from the core-hole lifetime and the self-energy. Typically, $\Gamma_{ch}+|\text{Im}\,\Sigma|$ is several electron volts at photoelectron energies above about 30 eV of an edge. This broadening limits the range probed by the photoelectron to clusters of the order of a few hundred atoms, and gives rise to a *short-range order* theory for energies above about 30 eV. Thus, long-range effects such as the sharp van Hove singularities of band structure calculations are naturally smeared out. Moreover, in this extended energy regime scattering is relatively weak and perturbation theory converges well. Conversely, in the near-edge regime (energies less than about 30 eV), the range is dominated mostly by the core lifetime $1/\Gamma_{ch}$, which is very long for low-Z materials or for very shallow edges. For those cases an intermediate- or long-range order theory may be needed, involving multiple scattering to all orders or very large clusters of atoms.

For polycrystalline materials or systems with cubic symmetry, only the diagonal terms in L and L' survive in Eq. (9), corresponding to couplings to various partial local, projected densities of states (LDOS) $\rho_l(E)$, i.e.,

$$S(\mathbf{q},\omega) \approx \sum_l (2l+1)|M_l(\mathbf{q},E)|^2\rho_l(E). \tag{14}$$

Thus, the dynamic structure factor is directly related to the LDOS. The coupling terms $M_l(q,E)$ are essentially atomic quantities which can be calculated theoretically to good accuracy. Thus, it may be possible to extract the LDOS $\rho_l(E)$ or the density matrix components $\rho_{L,L'}(E)$ from a sequence of experimental measurements of $S(\mathbf{q},\omega)$ at various $\mathbf{q}$ by a suitable inversion procedure of Eq. (13) or (14), regarded as a set of linear equations.

The propagator $G=G^c+G^{sc}$ naturally separates into intra-atomic contributions from the central atom G^c and from MS contributions from the environment G^{sc}. Thus, as in XAS, $S(\mathbf{q},\omega)$ can be factored as

$$S(\mathbf{q},\omega) = S_0(q,\omega)[1+\chi_{\mathbf{q}}(k)], \tag{15}$$

where $S_0(q,\omega)$ represents a smoothly varying atomic background, and $\chi_{\mathbf{q}}(k)$ is the "fine structure" due to multiple scattering from the environment. Here, we have also used a standard XAS notation, where $k=\sqrt{2(\omega+E_i)}$ is the photoelectron

wave number. The momentum transfer dependence of these two contributions to the dynamic structure factor can be analyzed separately as shown in detail below.

B. Central atom contribution

Much of the qualitative behavior of the spectra can be understood in terms of the central atom contribution (in the absence of other scatterers), which has been analyzed for isolated atoms by, e.g., Leapman *et al.*[37] This contribution is independent of the direction of the momentum transfer, and hence depends only on the magnitude q. For a condensed system, the states $R_L(\mathbf{r},E)=i^l R_l(r)Y_L(\hat{r})$, where $R_l(r)$ are radial wave functions and $Y_L(\hat{r})$ spherical harmonics, are scattering states defined for the potential of an "embedded" atom in the system. However, the deep core states differ little from those of isolated atoms, and spherical symmetry is still a good approximation. This yields the atomic background contribution

$$S_0(q,\omega)=\sum_l (2l+1)|M_l(q,E)|^2\rho_l^0(E), \tag{16}$$

where ρ_l^0 denote the diagonal matrix elements of the density matrix.

The matrix elements can be calculated by rotating the system so that the momentum transfer is along the z axis. Additionally, summing over the m quantum numbers of both the initial state and the final state partial waves and using properties of 3-j symbols, one finds[37]

$$|M_l(q,E)|^2=(2l_i+1)\sum_{l'}(2l'+1)\left|\begin{pmatrix} l_i & l' & l \\ 0 & 0 & 0\end{pmatrix}\right. \times\left.\int r^2 dR_l(r,E)j_{l'}(qr)R_i(r)\right|^2. \tag{17}$$

Since $j_{l'}(qr)\approx(qr)^{l'}$ near the origin, the dominant term for small q is the dipole approximation $l=1$. The first term in a power series expansion of $j_0(qr)$ cancels by orthogonality for $q\to 0$, and hence the first contributing terms of $j_{l'}(qr)$ from both $l'=0$ and $l'=2$ behave as $(qr)^2$. For large momentum transfers such that $qa>1$ and higher excitation energies, successively larger angular momentum ($l'>2$) excitation channels become more important. As a consequence, the behavior of $S_0(q,\omega)$ at increasing q reflects that of the LDOS of increasing l. This is illustrated in Fig. 1 for the background contribution $S_0(q,\omega)$. For EELS, however, experimental measurements of the double-differential cross section $d^2\sigma/d\Omega d\omega$ still tend to favor the dipole approximation due to the q^{-4} dependence of the electron scattering cross section $(d\sigma/d\Omega)_{e-e}$. Thus, most of the experimental signal in EELS is at small q.

C. Fine structure

From Eqs. (9) and (11), the normalized fine structure in the dynamic structure factor is given by

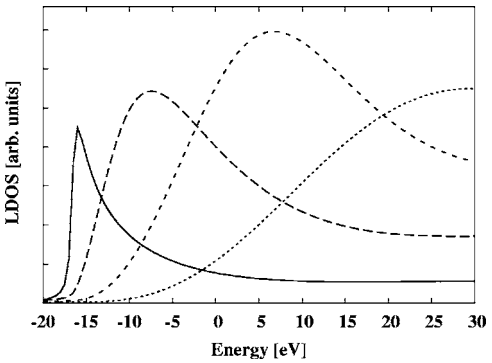

FIG. 1. LDOS $\rho_l^0(E)$ for the central site of fcc Al, in the absence of other scatterers: $l=0$ (solid); $l=1$ (long dashes); $l=2$ (dashes); and $l=3$ (short dashes). Note how the successive terms $\rho_l^0(E)$ with increasing angular momentum l peak at successively higher energies and overlap each other.

$$\chi_{\mathbf{q}}(k)=\frac{1}{S_0(\mathbf{q},\omega)}\sum_{LL'}M_L(-\mathbf{q},E)\rho_{L,L'}^{sc}(E)M_{L'}(\mathbf{q},E), \tag{18}$$

where $\rho_{L,L'}^{sc}(E)=(-1/\pi)\mathrm{Im}\,G_{L,L'}^{sc}(E)$. Clearly, the directional dependence of the spectra on $\hat{q}$ comes only from the scattering contribution, and naturally $\chi_{\mathbf{q}}(k)$ will change with the magnitude of the momentum transfer due to the $\mathbf{q}$ dependence of the coupling terms. This momentum transfer dependence of the near-edge structure has been used to study the symmetries of the core-excited states in solids.[6,13–18,22–25] It may also be possible to use this momentum transfer dependence to obtain information about intermediate- and long-range structure, which are contained in the EXAFS-type oscillations $\chi_{\mathbf{q}}(k)$.

One way of calculating the scattering contribution to the propagator G^{sc} for a big cluster of atoms is to use matrix inversion involving the free-particle propagator G^0 and the scattering matrix T, i.e.,[1]

$$G_{L,L'}^{sc}=e^{i\delta_l}[(\mathbf{1}-G^0T)^{-1}G^0]_{L,L'}e^{i\delta_{l'}}. \tag{19}$$

This representation is referred to as full multiple scattering (FMS), since it formally includes MS to all orders. FMS is often used to treat near-edge spectra where scattering is strong and the dimensions of the matrix $G_{L,L'}$ are relatively small. At higher energies or whenever the MS series converges well, the matrix $G_{L,L'}$ can alternatively be calculated in terms of a "path expansion," i.e., as a sum over all MS paths that a photoelectron can take away from the absorbing atom and back.[38] Formally, the path expansion is given by the sum

$$G_{L,L'}^{sc}=e^{i\delta_l}[G^0TG^0+G^0TG^0TG^0+\cdots]_{L,L'}e^{i\delta_{l'}}, \tag{20}$$

where the successive matrix products terms represent single-, double-, and higher order scattering processes. Remarkably, the path expansion has been found to be generally adequate for energies above about 30 eV of threshold, where of order 10^2 of the largest amplitude paths suffice to yield an accuracy of a few percent for most materials.[39]

Due to the large dimension $D \approx N(l_{max}+1)^2$ of the matrix $G_{L\mathbf{R},L'\mathbf{R}'}$, where N is the size of the cluster, exact calculations with the path expansion can only be carried out for a few, low-order MS paths. To overcome this bottleneck, an exact separable representation of the propagator was introduced by Rehr and Albers (RA)[39]

$$G^0_{L'\mathbf{R}',L''\mathbf{R}''} = \frac{e^{ikR}}{kR}\sum_{\lambda} Y_{L',\lambda}(k\mathbf{R}')\tilde{Y}_{\lambda,L''}(k\mathbf{R}''), \qquad (21)$$

where $R=|\mathbf{R}'-\mathbf{R}''|$ is the bond distance. The generalized spherical harmonic expansion coefficients $Y_{L',\lambda}$ and $\tilde{Y}_{\lambda,L''}$ converge rapidly in powers of $1/kR$, which is always $\ll$ unity for unoccupied states $k>k_F$, and hence this representation can be severely truncated. For FMS calculations the RA representation of the propagators in Eq. (21) is stable and converges rapidly. For the path expansion, the RA approach is exact for single scattering, and typically only six terms in λ suffice to give accuracies to the order of a percent or better over the typical range of wave numbers encountered in XAS experiment, $k_F \leqslant k \leqslant 20$ Å^{-1}, i.e., $E_F \leqslant E \leqslant 1500$ eV.

With the separable representation, one can sum over all intermediate angular momentum variables (l,m) at each site and define local *scattering matrices*. Then, the contribution $G^0TG^0T\cdots G^0$ to the total propagator from a given N-atom path $\Gamma \equiv [\mathbf{R}_1,\mathbf{R}_2,\ldots\mathbf{R}_N=\mathbf{R}_0]$ can be factored as a matrix product over small (typically 6×6) matrices[39]

$$F_{\lambda,\lambda'}(\boldsymbol{\rho},\boldsymbol{\rho}') = \sum_L \tilde{Y}_{\lambda,L}(\boldsymbol{\rho})t_l Y_{\lambda',L}(\boldsymbol{\rho}'),$$

which is the analog of the scattering amplitude $f(\theta)$ in plane-wave scattering theory, and a termination matrix $m^{\lambda_1,\lambda_N}_{L,L'}(\boldsymbol{\rho}_1,\boldsymbol{\rho}_N) = Y_{L,\lambda_1}(\boldsymbol{\rho}_1)\tilde{Y}_{L_N,\lambda_N}(\boldsymbol{\rho}_N)$, where $\boldsymbol{\rho}=k\mathbf{R}$.[39] For large L or L', it may be necessary to increase the dimension of λ in the termination matrices $m^{\lambda_1,\lambda_N}_{L,L'}$ beyond 6 for adequate convergence. Specifically, we obtain for each path (cf. Ref. 39),

$$G^{\Gamma}_{L,L'} = \frac{e^{i(\rho_1+\rho_2+\cdots\rho_N+\delta_l+\delta_{l'})}}{\rho_1\rho_2\cdots\rho_N}\sum_{\{\lambda\}} m^{\lambda_1,\lambda_N}_{L,L'}(\boldsymbol{\rho}_1,\boldsymbol{\rho}_N) \times [F_{\lambda_N,\lambda_{N-1}}(\boldsymbol{\rho}_N,\boldsymbol{\rho}_{N-1})\cdots F_{\lambda_2,\lambda_1}(\boldsymbol{\rho}_2,\boldsymbol{\rho}_1)]. \qquad (22)$$

In our code, the dependence on the bond vectors $\boldsymbol{\rho}$ and $\boldsymbol{\rho}'$ is simplified using rotation matrices and Euler angles. This expression is similar to the one used for analysis of XAS using path expansion.[1] In contrast to the case for XAS, which is dominated by the dipole approximation, however, all angular momentum channels now contribute with $\mathbf{q}$-dependent couplings. Thus, the fine structure from the path expansion can be written as

$$\chi_{\mathbf{q}}(k) = -\,\mathrm{Im}\sum_{\Gamma}\frac{e^{i(\rho_1+\rho_2+\cdots\rho_N)}}{\rho_1\rho_2\cdots\rho_N}\sum_{\{\lambda\}} H^{\lambda_1,\lambda_N}(\boldsymbol{\rho}_1,\boldsymbol{\rho}_N,\mathbf{q}) \times [F_{\lambda_N,\lambda_{N-1}}(\boldsymbol{\rho}_N,\boldsymbol{\rho}_{N-1})\cdots F_{\lambda_2,\lambda_1}(\boldsymbol{\rho}_2,\boldsymbol{\rho}_1)], \qquad (23)$$

where

$$H^{\lambda_1,\lambda_N}(\boldsymbol{\rho},\boldsymbol{\rho}_N,\mathbf{q}) = \frac{1}{S_0(q,\omega)}\sum_{L,L'} e^{i(\delta_l+\delta_{l'})} \times M_L(-\mathbf{q})m^{\lambda_1,\lambda_N}_{L,L'}(\boldsymbol{\rho}_1,\boldsymbol{\rho}_N)M_{L'}(\mathbf{q}). \qquad (24)$$

Note that only the coupling terms $H^{\lambda_1,\lambda_N}(\boldsymbol{\rho}_1,\boldsymbol{\rho}_N,\mathbf{q})$ depend on $\mathbf{q}$, while the scattering contribution is a product of low-order scattering matrices $F_{\lambda,\lambda'}$ which are dependent only on the material. When the dominant contribution comes from the dipole limit $l=l'=1$, the dependence on $\hat{\mathbf{q}}$ has the form $(\hat{\mathbf{q}}\cdot\hat{\mathbf{R}}_1)(\hat{\mathbf{q}}\cdot\hat{\mathbf{R}}_N)$. This form emphasizes paths beginning or ending in the direction $\hat{\mathbf{q}}$, and acts like a "searchlight" in probing the structure of a system. For polycrystalline materials or for measurements averaged over all $\hat{\mathbf{q}}$, this dependence averages out. Similarly, the contributions from the higher angular momenta couplings probe other symmetries.

By defining a $\mathbf{q}$-dependent *effective scattering amplitude* $f_{\mathrm{eff}}(\mathbf{q},k)$, one can use the path expansion [Eq. (23)] to express the fine structure $\chi_{\mathbf{q}}(k)$ in a form identical to the original EXAFS equation

$$\chi_{\mathbf{q}}(k) = s_0^2\sum_{\Gamma}\frac{|f_{\mathrm{eff}}(\mathbf{q},k)|}{kR^2}\sin(2kR+\Phi_k)e^{-2R/\lambda_k}e^{-2\sigma^2k^2}, \qquad (25)$$

where $k=\sqrt{2(\omega+E_i)}$, $R=(1/2)\Sigma_i R_i$ is the *effective path length*, and the prefactor $s_0^2 \approx 0.9$ is a many-body amplitude factor which accounts for inelastic losses (satellite excitations) beyond the quasiparticle approximation.[26] Here, the effects of thermal and structural disorder are included using a configurational average of Eq. (23). These damping effects can be approximated by a Debye-Waller factor $\exp(-2\sigma^2k^2)$, where σ^2 is the correlated mean-square variation $\langle(\delta R)^2\rangle$ for each scattering path,[1] while anharmonic terms from the first and third cumulants are generally weaker and contribute to the phase. Typically σ^2 is of order 10^{-2}–10^{-3} Å^2. For the case of full multiple scattering at low energies, these effects can be calculated to a good approximation by including a similar Debye-Waller factor $\exp(-\sigma^2k^2)$ in each propagator $G_{L\mathbf{R},L'\mathbf{R}'}(k)$; this ensures that the Debye-Waller factors for the dominant single-scattering paths agree with those for the path expansion. Finally, close to an absorption edge where k is small, the Debye-Waller factors are of order unity and can be ignored, except in cases where dipole forbidden transitions become allowed due to vibronic coupling.[40] In practical calculations $\sigma^2(T)$ can be approximated to reasonable accuracy using the correlated Debye model evaluated for the Debye temperature Θ_D of a material.[1] For other methods of treating multiple-scattering Debye-Waller factors, see for example, Filipponi *et al.*[41] A more general discussion is given by Fujikawa.[42]

III. EXAMPLES

A. Be *K* edge

As mentioned above, the momentum transfer magnitude q and directional $\hat{\mathbf{q}}$ dependence of the K edge in Be metal was measured and analyzed by Sternemann *et al.*[18] They found

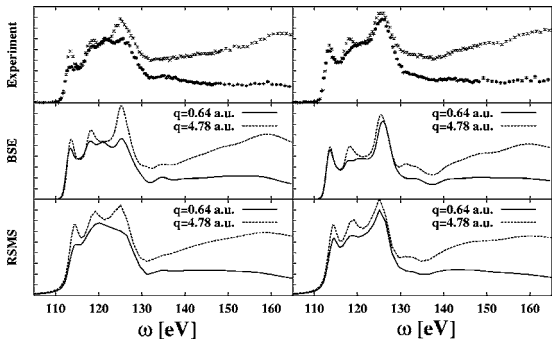

FIG. 2. Comparison between experiment (Ref. 18) (top panels) and inelastic loss spectra calculated using the BSE (middle panels) and the RSMS method of this work (lower panels) for the Be K edge. The spectra are shown for $\mathbf{q}$ perpendicular to the c axis (left panels), and $\mathbf{q}$ along the c axis (right panels). Spectra are shown for two values of momentum transfer q as indicated in the figure labels. The theoretical spectra was shifted by 4.5 eV to align with the experimental edge.

that the main changes in the spectra with increasing q could be explained by the increasing contribution from monopole (s-to-s)-type excitations. This leads to a net decreasing anisotropy, i.e., decreasing dependence on $\hat{\mathbf{q}}$ of the edge, since s-type states naturally have no directional dependence. This conclusion is supported by ground-state local density of states calculations using full-potential linear-augmented plane-wave and excited state calculations using the BSE method of Ref. 32.

In Fig. 2 we compare the inelastic scattering spectra calculated with the approach of this paper for the Be K edge with the experimental results of Ref. 18. From this comparison it is clear that our present calculation is capable of reproducing both the momentum transfer direction and magnitude dependence of the dynamic structure factor. However, there are noticeable discrepancies in some fine details in the spectra within the first 15 eV. For the momentum transfer perpendicular to the c axis, the 120 eV features are more pronounced in the RSMS calculation than in the experiment for both the low- and high momentum transfer. However, the main differences between these spectra are well reproduced by the present calculation. In the middle panel of Fig. 2 we show for comparison the results from the BSE method.[18,32] Considering how sensitive the problem of calculating core excitation is, the agreement between the two different theoretical methods is rather good. This serves to validate the one-electron, final-state rule calculations, at least for this case. As noted above, most of the differences occur rather close to the edge, which is also the region most sensitive to the details of the core hole-electron interaction and to the nature of the scattering potentials. Beyond the first 15 eV the agreement between the two methods is very good. For $\mathbf{q}$ along the c axis, agreement between the two calculations is also rather good for the energy range shown. For $\mathbf{q}$ perpendicular to the c axis, however, the comparison is somewhat mixed. For the first peak in the spectra, it appears that RSMS accurately predicts the experimental result. The difference is that the first peak becomes a shoulder at low momentum transfer and a peak at higher momentum

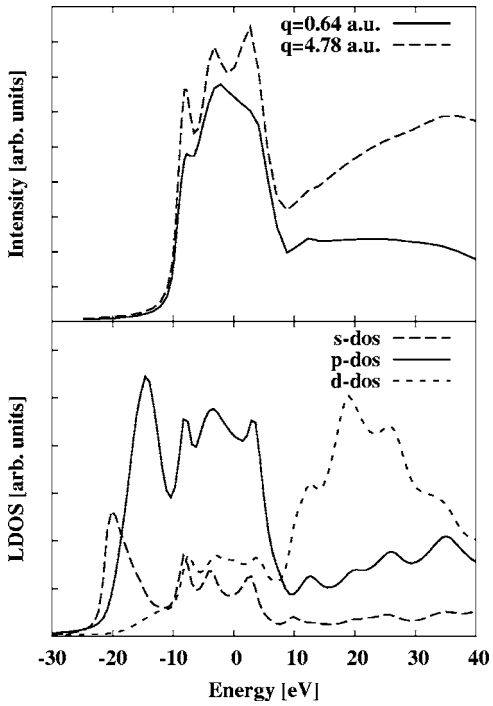

FIG. 3. Local projected DOS for Be together with inelastic scattering spectra for two values of momentum transfer q along the x axis. The Fermi level is at −9.4 eV.

transfer. On the other hand, the details of the spectra between 120–130 eV appear to be slightly better reproduced by the BSE.

As noted in Sec. II C, the momentum transfer-dependent changes in the spectra can be understood in terms of the changing weights of the different components of $\rho_{L,L'}(E)$ in the single-crystal case, and the LDOS $\rho_l(E)$ for polycrystalline systems. In Fig. 3 we show the s- p- and d-DOS for the core-excited state at the site of the core hole in Be metal. Also shown are the calculated inelastic scattering spectra for two values of momentum transfer along the x axis. The calculated spectra are shifted so that the Fermi energy is aligned with that obtained in the LDOS calculation, where $E=0$ is the vacuum level. On this scale the Fermi energy for Be as calculated by our RSMS code is $E_F=-9.4$ eV. The p-type LDOS close to the Fermi energy is composed of two peaks at −8 and +4 eV, and a broad shoulder at −4 eV. In the small momentum transfer regime the dipole limit is reached, and the general shape of the p-type LDOS is clearly shown in the shape of the calculated spectrum.The s-type LDOS, on the other hand, is composed of three sharp peaks at −8, −4, and +3 eV. Compared to the low-q spectrum, the high momentum transfer spectrum has sharp peaks at these same energies. The coincidence of the peaks is due to hybridization between the various angular momentum components. Clearly, the changes in the near-edge structure with increasing q can be attributed partly to the increasing contribution from the s-to-s-type transitions. Also, the changes due to the matrix elements that weight the different excitations have to be considered when comparing LDOS to experimental spectra. This can clearly be seen when comparing low momentum transfer spectra along either the x- or c axes. Although

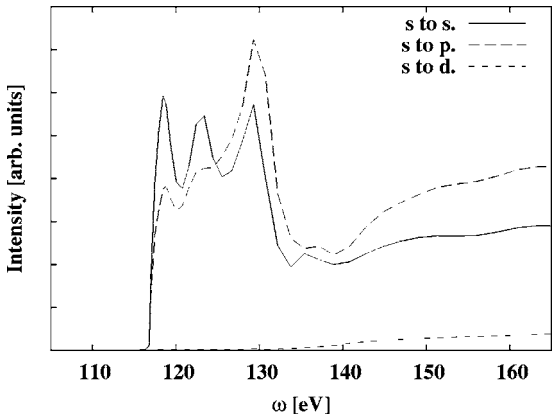

FIG. 4. Comparison of contributions to the inelastic loss spectra from monopole and dipole transitions, for momentum transfer $q=4.78$ a.u. along the c axis.

both exhibit a p-type LDOS structure, the weights of the different features are strongly dependent on the magnitude and direction of the momentum transfer. Also, the overlap of the different types (s vs p) of LDOS is clearly demonstrated in these results. The relative contributions to the sum of Eq. (14) from monopole (s-to-s), dipole (s-to-p), and quadrupole (s-to-d) transitions are illustrated in Fig. 4 for the higher momentum transfer $q=4.78$ a.u. along the c axis. At lower momentum transfer the contributions from the monopole transitions and quadrupole transitions are negligible. At this relatively high momentum transfer the dipole forbidden s-to-s transition is comparable in magnitude to the dipole allowed s-to-p transition. The s-to-d contribution is small at low energies but becomes increasingly important as the energy is increased, again reflecting the energy-dependent weight of different excitation channels.

The total spectrum changes also as function of the magnitude of the momentum transfer because of the changes in the channel-specific spectra. This change is due to the excitation energy E dependence of the final state partial wave, $R_L(\mathbf{r},E)$. As the momentum transfer changes, the matrix elements $M_L(\mathbf{q},E)=\langle R_L(E)|e^{i\mathbf{q}\cdot\mathbf{r}}|i\rangle$ make the channel (i.e., L)-specific spectra change at an energy E-dependent rate. In Fig. 5 the momentum transfer dependence of the dipole allowed and monopole (dipole forbidden) transitions is examined separately. The spectra are scaled so that the first peak for both momentum transfers is the same height. Besides this energy-independent scaling factor there is also a momentum transfer dependence on the shape of the channel specific spectra. At a qualitative level this change is mostly visible in the central atom contribution. The momentum transfer-dependent changes in the fine structure are less noticeable.

B. Al L_1 edge

As a final example we examine the core-excited states in fcc Al. The calculated x-ray absorption cross section and the dynamic structure factor for the L_1 edge at different momentum transfers are compared in Fig. 6. To make contact with $S(\mathbf{q},\omega)$, the absorption cross section $\sigma_{abs}(\omega)$ was

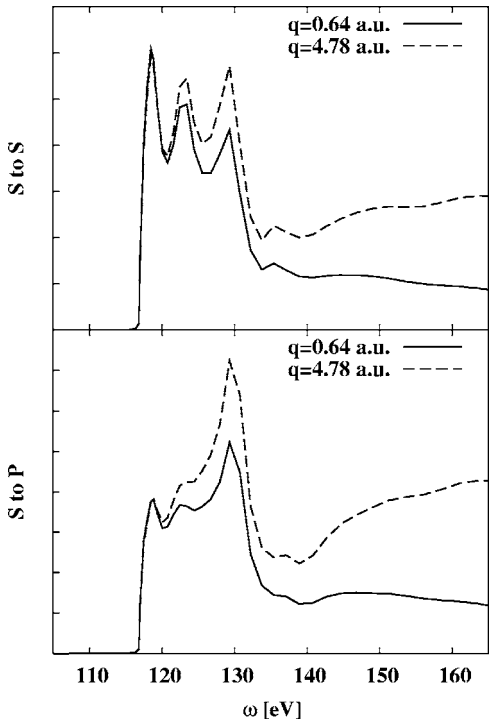

FIG. 5. Changes in the shape of different contributions to the Be K-edge spectra, as a function of the magnitude of the momentum transfer along the c axis for two values of q listed in the figure labels. The upper panel shows the changes for the monopole contribution and the lower panel, those for the dipole allowed transitions. The spectra were normalized so that the height of the first peak is the same for both values of q.

divided by the excitation energy, since in the limit $\mathbf{q}\to 0$ (Ref. 3)

$$\sigma_{abs}(\omega) \propto \omega S(\mathbf{q},\omega). \tag{26}$$

Comparison of $\sigma_{abs}(\omega)/\omega$ and $S(\mathbf{q},\omega)$ for $q=0.24$ a.u. clearly shows the well-known and experimentally verified[4]

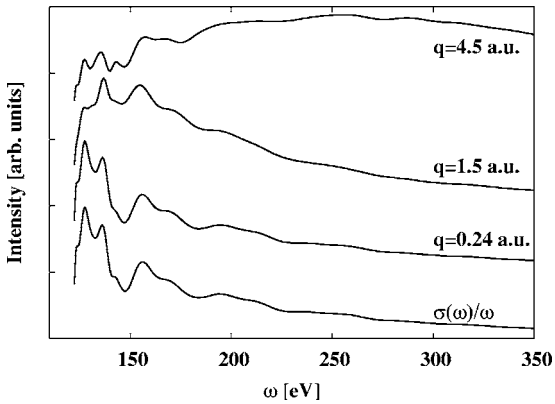

FIG. 6. Comparison of inelastic scattering and x-ray absorption spectra at the Al L_1 edge using the path expansion for several values of momentum transfer as indicated in the figure labels; the curve $\sigma(\omega)/\omega$ is the result for $q=0$. For clarity, the inelastic scattering spectra were slightly shifted vertically. All the spectra were scaled to be shown on the same figure.

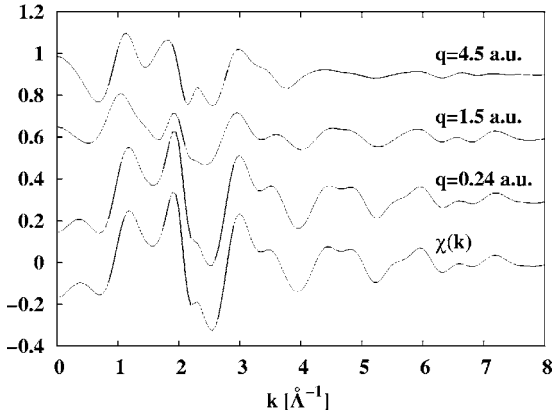

FIG. 7. Fine structure $\chi_{\mathbf{q}}(k)$ for Al at the L_1 edge for different values of momentum transfer as listed in the figure labels, together with the x-ray absorption fine structure $\chi(k)$, i.e., $q=0$. The curves are shifted for clarity.

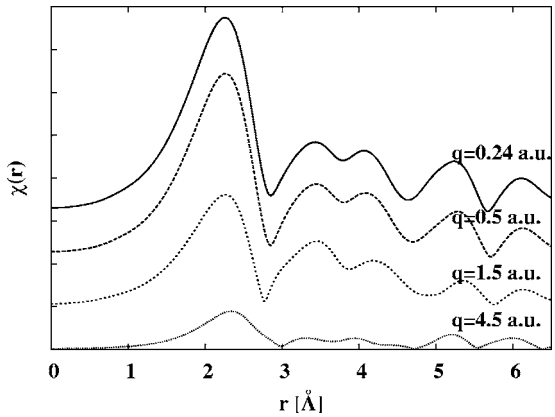

FIG. 8. Fourier transform of Al fine structure for several values of momentum transfer as listed in the figure labels. The differences reflect the interference between different channels contributing to the spectra.

fact that inelastic scattering results at low momentum transfer can be used to obtain the same EXAFS information as in XAS. Since we are interested in discussing the general trends of the momentum transfer dependence of $S_i(\mathbf{q},\omega)$ in the extended energy range, we have not included the Al $L_{2,3}$ edge (edge located at about 80 eV) in this theoretical demonstration. For comparison with momentum transfer-dependent experiments for this energy range (we are not aware of such experiments in any material), one would need to include these edges. As q is increased to $q=1.5$ and 4.5 a.u., the overall shape of the spectra changes. As mentioned above, this change is mostly due to changes in the central atom contribution. Although the EXAFS-like oscillations appear to diminish with higher momentum transfer, most of the broad oscillatory structure remains.

In Fig. 7 we examine the momentum transfer dependence of the **q**-dependent fine structure $\chi_{\mathbf{q}}(k)$. Here, we show the XAS fine structure $\chi(k)$, together with $\chi_{\mathbf{q}}(k)$ for several values of q at the Al L_1 edge. Again, it is clear that for low q the XAS result is reproduced. When the momentum transfer is increased, however, the shape of the fine structure of the spectra is modified in a way that cannot be explained by simple scaling factors, due to the mixture between the various angular momentum contributions. The changes are perhaps strongest close to the edge (at small k), but even the high-k spectra are modified. This suggests that it may be desirable to decompose the spectra into the various angular momentum components $\chi_l(k)$ prior to additional analysis. This is further illustrated in Fig. 8, which shows the Fourier transform of the EXAFS χ_q in R space, phase corrected by the dominant central atom p-wave phase shift $\exp(2i\delta_1)$. Such Fourier transforms have peaks close to the near-neighbor distances and provide a characterization of the near-neighbor radial structure. Thus, they can be used for quantitative fits of EXAFS in R space. Note that for small q the transform is insensitive to q but becomes substantially more complex for the larger values due to the overlapping contributions from the various channels.

IV. CONCLUSIONS

We have shown how the real-space multiple-scattering (RSMS) approach can be applied to model nonresonant inelastic scattering from deep core levels for arbitrary condensed systems over a broad spectral range. The approach is a generalization to finite momentum transfer of that used to model XAS based on the independent electron approximation and the final-state rule. In contrast to XAS, where dipole selection rules apply, couplings to all angular momentum components are important and hence can probe different symmetries of the excited states. Comparison of our approach with earlier work[18,32] based on the particle-hole BSE for the case of Be K edge gives a good agreement between these two methods. More generely the final-state rule approach used here and the BSE method have been compared both theoretically and in terms of practical implementation in Refs. 30 and 33. These studies and current results suggest that an effective one-electron treatment that includes the core hole via the final-state rule can often be adequate for calculations of inelastic scattering much the same way it is for XAS. We have also discussed how the results may be used to analyze the inelastic x-ray (XRS) or electron scattering (EELS) from core electrons. In particular, we discussed the relation between these spectra and the angular momentum projected density of states (e.g., s-type and p-type LDOS) and density matrix components $\rho_{L,L'}(E)$, and how these can be extracted from a series of experimental measurements. Our calculated spectra are compared with the experimental XRS results[18] for the case of the Be K edge, and give good agreement over a wide energy range, both for the directional and magnitude dependence of the momentum transfer. In addition, we have shown that the calculations reproduce the well-known and demonstrated relationship between XAS and nonresonant inelastic scattering at low momentum transfers, i.e., the dipole limit ($q\rightarrow 0$). An explicit example is given for the case of the Al L_1 edge. Finally, we have also discussed the momentum transfer dependence of the fine structure $\chi_{\mathbf{q}}(k)$ in the EXAFS region, and suggested how this might be exploited in structural studies.

ACKNOWLEDGMENTS

We thank K. Hämäläinen, G. Hug, E. L. Shirley, S. Manninen, and J. Seidler for useful discussions. We would also like to thank C. Sternemann for discussions and for giving us the experimental data for Be *K* edge in numerical form. This work was supported in part by the U. S. Department of Energy, Grant No. DE-FG06-97ER45623, and by NIST, and was facilitated by the DOE Computational Materials Sciences Network. J.A.S was supported by the Academy of Finland (Grant No. 201291/40732).

[1] J. J. Rehr and R. C. Albers, Rev. Mod. Phys. **72**, 621 (2000).
[2] A. L. Ankudinov, B. Ravel, J. J. Rehr, and S. D. Conradson, Phys. Rev. B **58**, 7565 (1998).
[3] Y. Mizuno and Y. Ohmura, J. Phys. Soc. Jpn. **22**, 445 (1967).
[4] T. Suzuki, J. Phys. Soc. Jpn. **22**, 1139 (1967).
[5] M. Inokuti, Rev. Mod. Phys. **43**, 297 (1971).
[6] J. J. Ritsko, S. E. Schnatterly, and P. C. Gibbons, Phys. Rev. B **10**, 5017 (1974).
[7] S. Doniach, P. M. Platzman, and J. T. Yue, Phys. Rev. B **4**, 3345 (1971).
[8] W. Schülke, *Handbook of Synchrotron Radiation*, edited by G. S. Brown and D. E. Moncton (North-Holland, Amsterdam, 1991), Vol. 3.
[9] K. Hämäläinen and S. Manninen, J. Phys.: Condens. Matter **13**, 7539 (2001).
[10] See, e.g., W. Jones and N. H. March, *Theoretical Solid State Physics* (Wiley-Interscience, London, 1973), Vol. 1.
[11] C. Sternemann, J. A. Soininen, S. Huotari, G. Vankó, M. Volmer, J. S. Tse, and M. Tolan, Phys. Rev. B **72**, 035104 (2005).
[12] U. Bergmann, P. Glatzel, and S. P. Cramer, Microchem. J. **71**, 221 (2002).
[13] M. H. Krisch, F. Sette, C. Masciovecchio, and R. Verbeni, Phys. Rev. Lett. **78**, 2843 (1997).
[14] K. Hämäläinen, S. Galambosi, J. A. Soininen, E. L. Shirley, J.-P. Rueff, and A. Shukla, Phys. Rev. B **65**, 155111 (2002).
[15] J. A. Soininen, K. Hämäläinen, W. A. Caliebe, C.-C. Kao, and E. L. Shirley, J. Phys.: Condens. Matter **13**, 8039 (2001).
[16] Y. Feng, G. T. Seidler, J. O. Cross, A. T. Macrander, and J. J. Rehr, Phys. Rev. B **69**, 125402 (2004).
[17] H. Nagasawa, S. Mourikis, and W. Schülke, J. Phys. Soc. Jpn. **58**, 710 (1989).
[18] C. Sternemann, M. Volmer, J. A. Soininen, H. Nagasawa, M. Paulus, H. Enkisch, G. Schmidt, M. Tolan, and W. Schülke, Phys. Rev. B **68**, 035111 (2003).
[19] M. Tomellini and P. Ascarelli, Solid State Commun. **72**, 371 (1989).
[20] T. Fujikawa, *Handbook of Thin Film Materials*, edited by H. S. Nalwa (Academic Press, San Diego, 2002), Vol. 2, Chap. 9.
[21] A. P. Hitchcock, J. Electron Spectrosc. Relat. Phenom. **112**, 9 (2000).
[22] J. R. Fields, P. C. Gibbons, and S. E. Schnatterly, Phys. Rev. Lett. **38**, 430 (1977).
[23] N. Jiang and J. C. H. Spence, Phys. Rev. B **69**, 115112 (2004).
[24] R. F. Klie, H. Su, Y. Zhu, J. W. Davenport, J.-C. Idrobo, N. D. Browning, and P. D. Nellist, Phys. Rev. B **67**, 144508 (2003).
[25] N. Jiang, B. Jiang, J. C. H. Spence, R. C. Yu, S. C. Li, and C. Q. Jin, Phys. Rev. B **66**, 172502 (2002).
[26] L. Campbell, L. Hedin, J. J. Rehr, and W. Bardyszewski, Phys. Rev. B **65**, 064107 (2002).
[27] C. R. Natoli, M. Benfatto, C. Brouder, M. F. Ruiz Lopez, and D. L. Foulis, Phys. Rev. B **42**, 1944 (1990).
[28] P. Krüger and C. R. Natoli, Phys. Rev. B **70**, 245120 (2004).
[29] A. L. Ankudinov, A. I. Nesvizhskii, and J. J. Rehr, Phys. Rev. B **67**, 115120 (2003).
[30] A. L. Ankudinov, Y. Takimoto, and J. J. Rehr, Phys. Rev. B **71**, 165110 (2005).
[31] E. L. Shirley, Phys. Rev. Lett. **80**, 794 (1998).
[32] J. A. Soininen and E. L. Shirley, Phys. Rev. B **64**, 165112 (2001).
[33] J. J. Rehr, J. A. Soininen, and E. L. Shirley, Phys. Scr., T **T115**, 207 (2005).
[34] W. L. Schaich, Phys. Rev. B **8**, 4028 (1973).
[35] L. Hedin and B. I. Lundqvist, J. Phys. C **4**, 2064 (1971).
[36] Without loss of generality, we have assumed here that **q** is along the Cartesian *z* axis.
[37] R. D. Leapman, P. Rez, and D. F. Meyers, J. Chem. Phys. **72**, 1232 (1980).
[38] P. A. Lee and J. B. Pendry, Phys. Rev. B **11**, 2795 (1975).
[39] J. J. Rehr and R. C. Albers, Phys. Rev. B **41**, 8139 (1990).
[40] A. L. Ankudinov and J. J. Rehr, Phys. Scr., T **T115**, 24 (2005).
[41] A. Filipponi, A. DiCicco, and C. R. Natoli, Phys. Rev. B **52**, 15122 (1995).
[42] T. Fujikawa, J. Phys. Soc. Jpn. **65**, 87 (1995).